Design and Analysis of Spiroid Wingtip

[1]Mariyam Naseer, [2]Dr. Khalid Pervaiz, [3]Mr. Muhammad Anwar
Department of Aeronautics & Astronautics
Institute of Space Technology, Islamabad, Pakistan
[1]emma.mary611@gmail.com

Abstract*— Improvement in aerodynamics of an aircraft while considering reduction of the required fuel consumption requires a proper design of wingtip devices to diffuse the strong vortices produced at the tip and thereby optimizing the span wise lift distribution. This research describes the influence of using a novel cross section (a hybrid of cambered and flat plate cross section) for the Spiroid tip with the wing of an aircraft model for reduction of induced drag without increasing the span of the aircraft. Aerodynamic characteristics for the aircraft model with and without Spiroid wingtip having Boeing 747-800 wing have been studied using computational techniques. The computational simulation had been carried out by FLUENT 6.2 solver using finite volume approach. Pressure differentials and vortices is checked at high subsonic Mach regimes as this is the flight regime of commercial aircrafts. Comparison of lift coefficient, drag coefficient and lift to drag coefficient has been made. It was found analytically that the wing with the Spiroid tip gives 5-6% reduction in fuel consumption as compared to the wing without any tip. Furthermore Spiroid tip with the newly suggested hybrid cross section is even more fuel efficient then the tips which had flat plates or cambered airfoil as cross section.

Keywords—Wing Tip Design; Computational Fluid Dynamics (CFD); Spiroid Wing Tip; Fluent

I. INTRODUCTION

In an era of rising fuel prices and environmental concerns, efforts to decrease fuel consumption and lower emissions are of profound interest to the aviation industry. In recent years there has been intense research and study into aerodynamic devices that provide commercial aircraft with longer range and more efficient rates of fuel consumption [1].

The improvements via the addition of winglets and winglet configurations have been implemented to various degrees of successes. A further optimization of a new breed of winglets configurations can increase the efficiency of the aircraft.

Two such wingtip devices that could maximize the range and minimize the fuel consumption of commercial aircraft are Endplates and wingtip. Spiroid wingtip devices have been shown to reduce wing loading, increase range, and improve fuel consumption of commercial aircraft. These benefits to an aircraft's performance are due to the ability of endplates and Spiroid wingtips to reduce the induced drag, generated by a three-dimensional (3-D) finite wing.

The force that acts on a wing to create lift is caused by a pressure differential between the lower and upper surfaces of the wing. The pressure on the lower surface of the wing is higher than that on the upper surface of the wing, creating a net lifting force normal to the freestream airflow. On a clean wing, this difference in pressure between the lower and upper surfaces of the wing causes air to flow from the lower surface to the upper surface of the wing at the wingtips. This produces a downwash onto the top of the wing, as illustrated in Fig. 1.

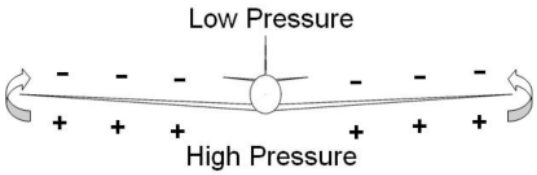

Figure 1: Pressure Distribution on Wing

The downwash of air onto the upper surface of the wing at the wingtip has the affect of vectoring the flow of air over the wing downward. This produces a new lift force (L') on the wing normal to this new velocity vector (V'). This concept is illustrated in Fig. 2. The lift force generated by the wing is no longer perpendicular to the freestream velocity (V_∞), and has a horizontal force component directed downstream of the flow. This horizontal force component is the induced drag (D_i).

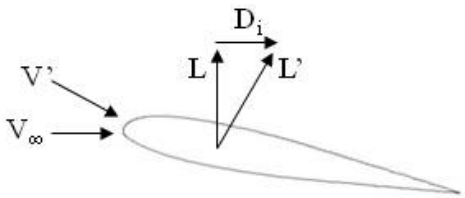

Figure 2: Velocity Vector and Induced Drag

The induced drag created by the downwash of airflow onto the upper surface of the wing at the wingtips produces vortices that trail in the aircraft's wake, causing drag. The fundamental premise of wingtip devices is to reduce the induced drag and consequently, the trailing vortex strength [3]. By minimizing the induced drag, and thus the wingtip vortices produced by an aircraft's wing, the energy required to create the tip vortices can be conserved and the total drag on the wing reduced.

The coefficient for the induced drag over a 3-D wing (C_{Di}) is given by the Eq. (1):

$$C_{Di} = \frac{C_L^{\,2}}{\pi e AR} \tag{1}$$

Where C_L is the lift coefficient, e is the Oswald efficiency factor, and AR is the aspect ratio. It is seen from Eq. (1) that

the induced drag over a finite wing is reduced by decreasing the C or increasing the AR. Winglets and Spiroid Winglet serve to increase the aspect ratio of a wing, thereby reducing the induced drag. However, disadvantages of winglets include an increase in the bending moment at the root of the wing and additional parasite drag.

A computational fluid dynamics (CFD) study of the vortex wake of a 3-D wing with dihedral, taper, and sweep at typical commercial aircraft cruise conditions was conducted. Two winglet devices–blended winglets and Spiroid wingtips–were modeled and their affect on the vortices in the wake region of the wing were studied. The results of the wingtip studies were then compared to a clean wing configuration.

Three different 3-D wing configurations were modeled using Creo software, and preprocessed using ICEM CFD meshing software. The generated meshes of the three 3-D wings were then imported into FLUENT CFD software for the numerical analysis and post-processing. Vorticity magnitude contour and vector plots for the three wing-configurations are presented in order to examine their affect on the vortex wake of each wing. The results obtained from the numerical simulation are discussed, and conclusions made.

II. 3-D Wing Geometry

Three wing-models were created for the computational analysis: a clean wing (no wingtip devices), a wing with blended winglets, and a wing with Spiroid wingtips. All of the geometric models used in the study were created using CREO software.

A wing with dihedral, taper, and sweep was modeled in order to accurately simulate the vortices in the wake region of a finite 3-D wing. The wing geometry used in this study also consisted of multiple airfoil sections, to add to the realism of the model. To preserve accuracy of the computational results, the airfoils used in the creation of the geometry of the wing were based on the airfoil sections used by conventional commercial airliners [4].

The 3-D wing geometries with blended winglets and Spiroid wingtips were derivations of the clean 3-D wing model. The 3-D wing with a blended winglet was created by adding on a winglet to the clean wing CREO model. In practice, the proper design of winglets is a precise and analytical exercise. For the purpose of this study, however, the design of the winglet was approximated.

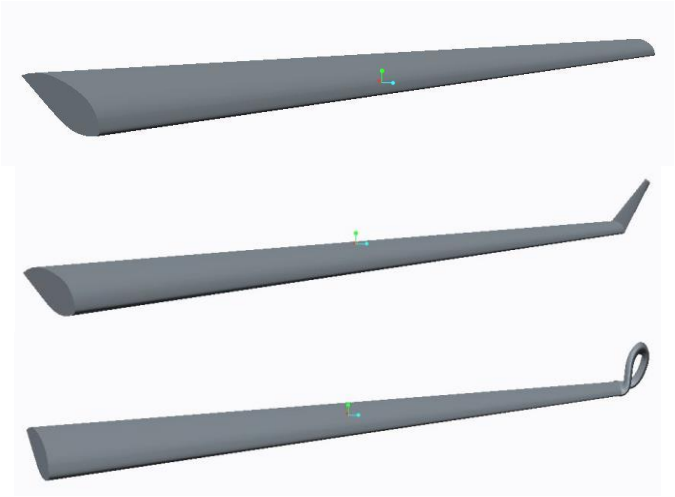

Figure 3: (a) Simple Wing (b) Winglet (c) Spiroid Wingtip

III. Pre-processing and Mesh Generation

The three wing models created in CREO were imported into ANSYS for pre-processing and meshing. The geometry files were saved and imported as step files (.stp) and scaled to 1/100 of their actual size. The same meshing process described in the following section was used with all three wing-models. The first step in creating a computational mesh was to create faces of the upper and lower surfaces of the 3-D wing and the flow domain. From these faces, two volumes were created: a wing volume and a domain volume. Next, the wing volume was subtracted from the domain volume using a Boolean operation.

The next step was to choose a meshing scheme for the wing and control volume. Traditional meshes involving 3-D wings are often created using a cooper structured mesh or a tetrahedral unstructured mesh scheme. However, because a cooper mesh projects a face mesh along an axis throughout a volume, the wing geometry would need to have constant airfoil cross-sections and little to no sweep or dihedral. Another consideration when meshing an aircraft wing is the employment of a boundary layer over the surface of the wing.

As a result of the complex geometry of the three wings used in this study, e.g., dihedral, sweep, different airfoils, and winglets, the most efficient mesh in terms of time and computational resources was created using the tetrahedral unstructured scheme, without a boundary layer.

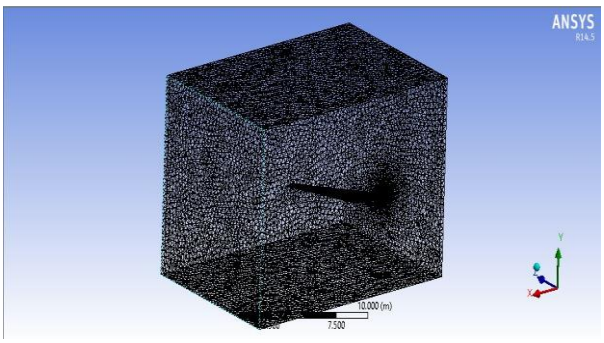

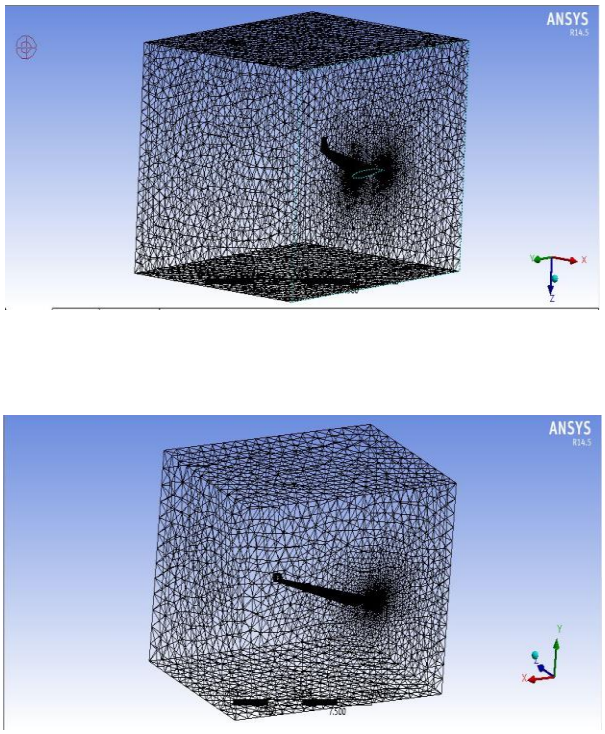

Figure 4: Meshing (a) Simple Wing (b) Winglet (c) Spiroid Winglet

IV. Numerical Processing and Solver Setup

After the generation of the 3-D mesh, the mesh was imported into the FLUENT 3-D solver. Although each 3-D wing mesh was different in terms of cell size and node count, the average number of cells in the final meshes were 2,763,000 and the average number of nodes were 515,000. After each 3-D wing mesh was imported into FLUENT, it was scaled to actual size to ensure the accuracy of the results. Next the solver, viscous model, material, boundary conditions, and solution were defined for the computational analysis.

The solver chosen for the computational analysis of all three wings was a second order implicit, unsteady solver. A double precision solver was chosen over the 3-D single precision solver. Next, the viscous model used for the computational analysis was defined.

The viscous model used for the computational analysis was the Spalart-Allmaras model. The Spalart-Allmaras model is a simplified, one-equation model that has proved to be successful in accurately modeling vortex and turbulent flows, such as those associated with the present study. Additionally, because of limitations with respect to CPU memory allocation, the employment of the Spalart-Allmaras viscous model provided for a faster solution convergence. Next, the material used for the computational analysis was defined.

All of the boundary condition values for pressure and velocity were based on conventional commercial aircraft cruise conditions. Boundary conditions were assigned for each of the six faces of the flow domain as well for the 3-D wing. The left face, or inlet, was defined as a 'pressure inlet'. The right face, or outlet, was defined as a 'pressure far field'. The top, bottom, root, and rear faces of the domain were each defined as 'symmetry'. Lastly, the wing, with all of its faces, was assigned as a 'wall' for the computational analysis.

The material for the numerical analysis in FLUENT was defined as air. The velocity at typical cruise conditions for jet airliners is Mach 0.85, therefore the density of the fluid was modeled as an ideal gas, as the flow at this speed cannot be assumed incompressible. For the material viscosity, a Sutherland approach was used to manage the viscous effects of the solution. Next, the boundary conditions for the flow domain were defined.

Because the numerical simulation involves a compressible flow solution, all the pressure values for the boundary conditions were set to gauge pressures to ensure the convergence of the solution. The inlet boundary condition of the flow domain was set to a value 21,728 Pa, corresponding to a cruise altitude of 30,000 feet. The outlet of the flow domain was defined with a pressure of 21,728 Pa and a Mach number of 0.85. To avoid any back flow across the computational domain during the solution, a turbulence intensity ratio of 1 was defined for both the pressure inlet and pressure far field boundary types. Next, the solver control for the solution of the computational analysis was defined.

A second order upwind discretization parameter was chosen for both the flow and turbulence intensity to improve the accuracy of the results of the solution. The courant number was reduced from 5 to a value of 2 to ensure convergence of the solution. The solver convergence criteria was then set.

After the convergence criteria for each independent 3-D wing case was set to 10^{-3}, the solver was initialized and the solution iterated. For each of the three CFD analyses conducted on the wing models, the solution converged after approximately 3000 iterations.

V. Post Processing and Results

FLUENT was used for post-processing of the results for each of the three wing configurations and flow domains. Following the convergence of the solution for each case, the vorticity magnitude and vorticity vectors of the flow field behind the wing were examined. The axial velocity in the core of the vortex wake was also plotted for each 3-D wing configuration.

By creating plane surfaces in FLUENT, the contours of the vorticity magnitude in the vortex wake region of the flow was visualized. Following figure show a side view of the contours of vorticity magnitude in s^{-1} for the clean wing, the wing with winglet, and the wing with Spiroid wingtips, respectively. The contours of vorticity magnitude denoted by red represent magnitudes of vorticity in the wake region of the wing at 25 s^{-1}.

A comparison between the three wing configurations in Fig. 5 shows that the wing with winglets configuration had the highest vorticity magnitude immediately aft of the wingtips, followed by the clean wing and the wing with Spiroid wingtips configurations. The trailing vortex of the wing with winglets configuration was also greater in length than the clean wing and the Spiroid wingtip configurations. Of the three contour plots it was Fig. 5c, which represented the Spiroid wingtip configuration, that depicted a lower overall vorticity magnitude as well as a shorter trailing vortex than the other two configurations.

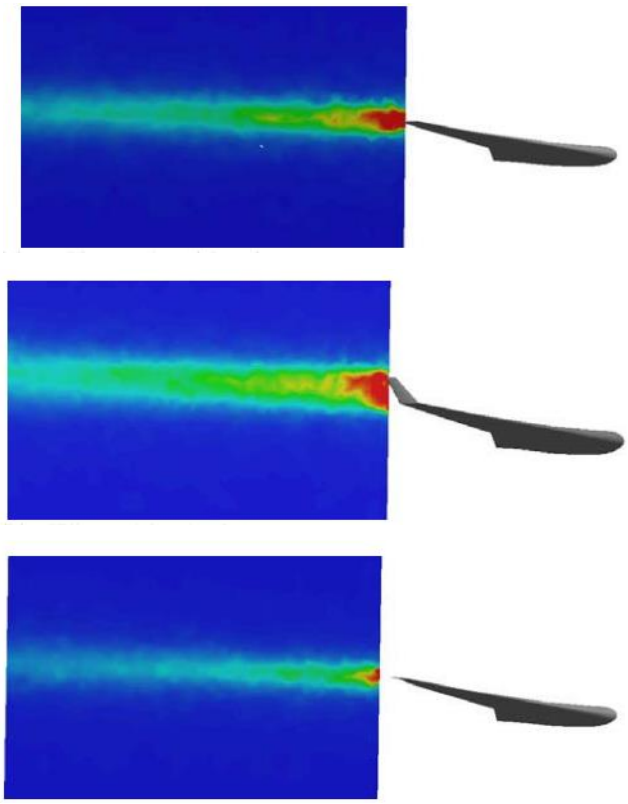

Figure 5: Contour of Vorticity magnitude, 25 s^{-1}

From examination of Fig. 5, the wing with Spiroid wingtip configuration produced the lowest overall vorticity magnitude corresponding to the lowest induced drag, when compared to Fig. 5a and Fig 5b. The largest vorticity magnitude was produced by the wing with winglets configuration, shown in Fig. 5b. However, an investigation of the vorticity magnitude from a different vantage point was needed to verify these initial findings.

Figure 6 shows a planform view contour plot of the vorticity magnitude for each wing configuration. The clean wing, wing with winglets, and wing with Spiroid wingtips configurations are shown in Fig. 6a, Fig. 6b, and Fig. 6c, respectively. The vorticity magnitude in the wake region of each wing configuration is highest just aft of the wingtip and decreases in magnitude as the distance downstream of the wingtip increases, as expected. The clean wing configuration displayed the highest overall vorticity both in the direction of the flow and in the span-wise direction. Figure 6a shows that the progression of the vortex wake inboard of the wingtips on the clean wing configuration effectively decreases the AR of the wing, increasing the induced drag over the wing.

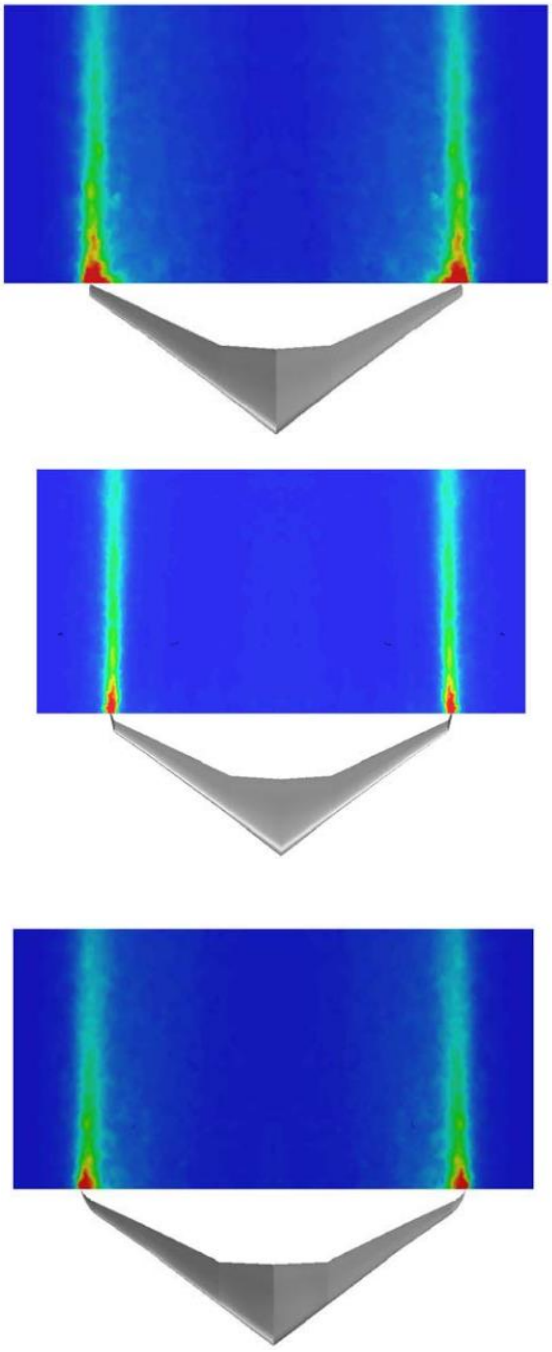

Figure 6: Contour of Vorticity magnitude, 25 s^{-1}

The wing with winglets configuration, Fig.6b, displayed a high vorticity magnitude throughout the wake region. However, the vortex wake for the wing with winglets configuration had the lowest vorticity in the span-wise direction when compared to the clean wing and wing with Spiroid wingtips configurations. By minimizing the vortex flow inboard of the wingtips, the AR of the wing is conserved, minimizing the induced drag over the wing. Additionally, the vortex wake of the wing with winglets configuration was more concentrated than the other two wing-configurations, indicating that the energy of the vortex wake was conserved. By conserving and focusing the energy of the vortex wake aft of the aircraft, a component of thrust in the forward direction of flight would result.

The wing with Spiroid wingtips configuration, Fig. 6c, had the lowest overall magnitude of vorticity in the wake region. Both in the direction of the flow and in the span-wise direction, the overall vorticity magnitude was smaller than that of the clean wing and wing with wingtips configurations. Similar to the wing with winglets, the vortex flow inboard of the wingtips caused by the Spiroid wingtip configuration effectively conserves the AR of the wing, thereby minimizing the induced drag on the wing. Additionally, the effect of the Spiroid wingtips on the vortex wake was to minimize the overall vorticity magnitude and thus the vortex drag.

To further study the vortex strength generated by the wingtip for each case, the vorticity vectors were examined. The vorticity vectors for each 3-D wing configuration were displayed at the same scale. In this way, the vector magnitudes of the three wing configurations could be directly compared. Vectors of vorticity magnitude at the wingtip region for the clean wing, wing with winglets, and wing with Spiroid wingtips are shown in Fig. 7a, Fig. 7b, and Fig. 7c, respectively. The variations in the magnitudes of the vorticity vectors are represented by the size of the vector heads–the larger the vector head the greater the magnitude. The vorticity vector magnitudes displayed in Fig. 7 range from 5-25 s^{-1}.

The vectors of vorticity magnitude for each of the three wing-configurations are concentrated at the wingtip region and flow in a clockwise direction from the lower surface of the wing to the upper surface of the wing, as expected. It is seen from the clean wing configuration in Fig. 7a that the vectors of vorticity of the clean wing are considerably larger in magnitude than those of the winglet and Spiroid wing configurations.

The wing with winglets configuration displayed lower vorticity vector magnitudes at the wingtips than that of the clean wing, and higher vorticity vector magnitudes than the wing with Spiroid wingtips. Inspection of Fig. 7b shows that as the air from the lower surface (at a higher pressure) flows around the wingtip to the upper surface (at a lower pressure), the winglet configuration effectively reduced the magnitude of the wingtip vortex thereby reducing the induced drag on the wing.

The Spiroid wingtip configuration, shown in Fig. 7c, displayed the lowest overall vorticity vector magnitudes as denoted by the relatively small vector heads in the figure. It is also seen in Fig. 7c that the wing with Spiroid wingtips configuration has fewer vectors associated with the wingtip vortices when compared to both the clean wing and wing with winglets configurations. Fewer vorticity vectors suggests that a weaker vortex wake was generated by the Spiroid wingtip configuration, resulting in less induced drag on the wing.

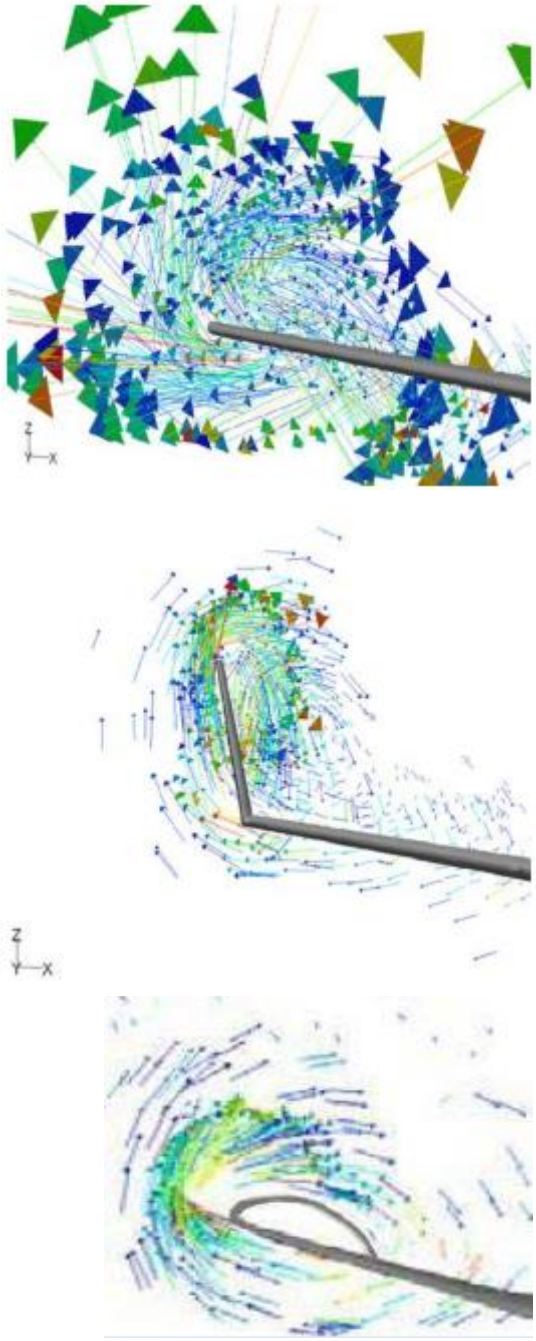

Figure 7: Vectors of Vorticity Magnitude at wingtips, 25s^{-1}

The results obtained from both the vorticity vector plots and contour plots coincide with respect to the overall vorticity magnitudes generated by the three wing-configurations represented in this study.

Investigating further, the vector field of the trailing vortex wake produced by the different winglet devices were analyzed.

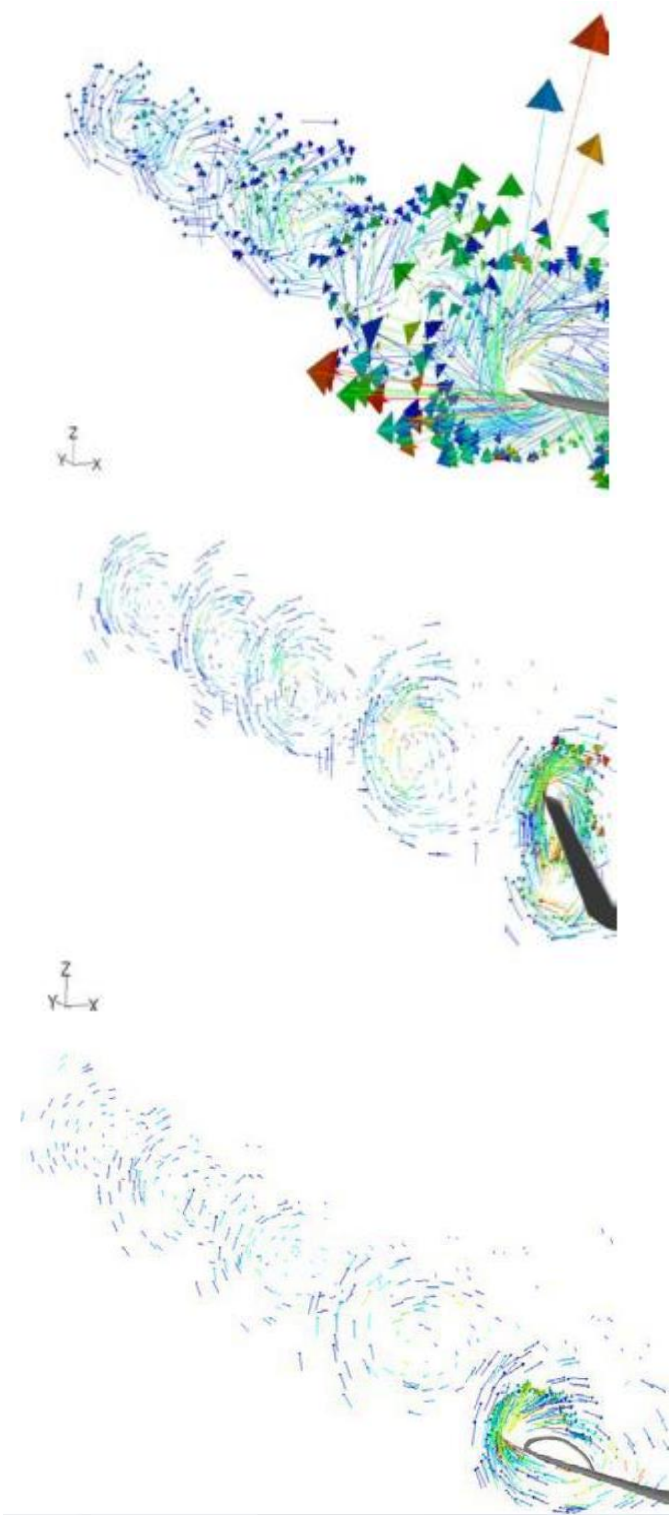

Figure 8: Vectors of vorticity magnitude in wake region, 25s^{-1}

The vector field of the vortex wake for the clean wing, wing with winglets, and wing with Spiroid wingtips configurations are shown in Fig. 8a, Fig. 8b, and Fig. 8c, respectively. Of particular significance are the large vorticity vector magnitudes present throughout the vortex wake of the clean wing configuration in comparison to the wing with winglets and wing with Spiroid wingtips configurations. The 3-D wing model with winglets produced a relatively large magnitude and continuous vortex wake as well, but the vector field was more concentrated than that of the clean wing. The core of the vortex wake in Fig. 8b is yellow in color, denoting a vorticity magnitude in this region of the vortex wake of approximately 15 s^{-1}. This validates an earlier finding that the vortex wake generated by the wing with winglets configuration conserved the otherwise wasted energy in the vortex wake by focusing the wingtip vortices into a strong jet of air that produces a component of thrust in the forward direction.

Of the three wing-configurations, the wing with Spiroid wingtips exhibited the lowest vorticity vector magnitudes throughout the vortex wake. Unlike the other wing cases, the strength of the vortex wake of the wing with Spiroid wingtips gradually decreased as the distance downstream of the wingtip increased. By reducing the overall magnitude of the vortex wake, the wing with Spiroid wingtip configuration effectively reduces the induced drag on the wing.

The vorticity of the vortex wake for each wingtip is plotted in Fig. 9. The range of the plot extends from the wingtip of each wing to the boundary of the flow domain, in the direction of the freestream. The plot indicates that the vorticity associated with the clean wing and the wing with winglets configurations share a similar flow pattern. However, upon closer inspection of the plot the vorticity magnitude in the vortex wake of the clean wing is more erratic and turbulent than for the wing with winglets. As illustrated in the contour plots, the wing with winglets configuration produces strong wingtip vortices, however they are less turbulent and more concentrated than the clean wing configuration. This characteristic allows winglets to produce a component of force in the thrust direction of the aircraft.

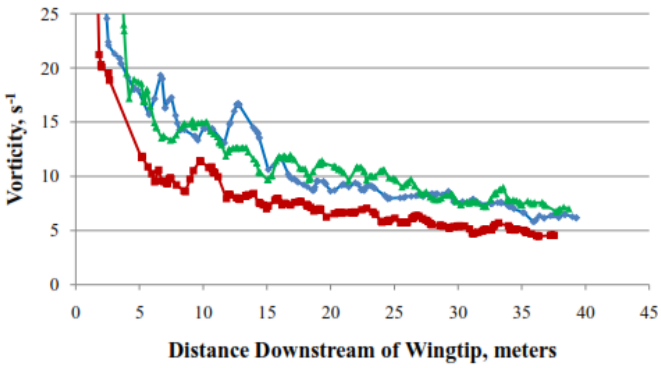

Figure 9: Vorticity in the vortex wake region

VI. Conclusion

The present study serves as a preliminary investigation into the aerodynamic effects of different wingtip configurations on the wingtip vortices generated as a result of the induced drag on a wing. In addition, the advantages and disadvantages of 3-D finite wings with winglets and Spiroid wingtip wing configurations were investigated. The results presented in this study reveal two methods for reducing wingtip vortices and, consequently, the induced drag on a 3-D wing.

This study has shown that clean wing configurations, i.e., wings without wingtip devices, produce the highest vorticity magnitudes when compared to wing configurations that

employ either winglets or Spiroid wingtip designs. The vortex wake generated by clean wing configurations reduce the aspect ratio of the wing, thereby increasing the induced drag on the wing. The winglet design employed in this study demonstrate the potential to produce a component of force in the thrust direction of the aircraft by concentrating the otherwise turbulent and chaotic vortex flow behind the wingtips into a more energy-efficient flow, thereby counteracting the drag on the wing. Alternatively, Spiroid wingtips reduce the overall magnitude of the tip vortices, thereby reducing the induced drag on the wing. The streamline design of the Spiroid wingtips provide less resistance to the flow over the wingtips and, in this way, conserve the energy of the flow.

The results of this preliminary study suggest that wings designed with winglets or Spiroid wingtips can indeed reduce the induced drag on a wing during cruise conditions. This reduction of the induced drag on an aircraft's wing offer advantages in terms of an aircraft's performance including improved fuel efficiency, increased range, and reduced wing loading.

Future studies could be conducted to more accurately model the flow around these wingtip devices. Accurate coefficients of lift and drag can be obtained through wake-momentum analysis methods as used in other studies

Furthermore, a more accurate method of generating the geometry for the winglet and Spiroid wingtip devices is necessary. Future studies that investigate the effects of these wingtip devices at various angles of attack would provide better insight into their aerodynamic benefits as well.

VII. References

[1] van Dam, C., Holmes, C., and Pitts, C. "Effects of Winglets on Performance and Handling Qualities of General Aviation Aircraft", AIAA Aircraft Systems Meeting, AIAA, Anaheim, CA. 1980. J. Clerk Maxwell, A Treatise on Electricity and Magnetism, 3rd ed., vol. 2. Oxford: Clarendon, 1892, pp.68-73.

[2] de Mantos, B., Macedo, A., and da Silva Filho, D. "Considerations about Winglet Design", AIAA 21st Applied Aerodynamics Conference, AIAA, Orlando, Florida, 2003.

[3] Gold, N., Visser, K. "Aerodynamic Effects of Local Dihedral on a Raked Wingtip", AIAA 40th Aerospace Sciences Meeting and Exhibit, AIAA, Reno, NV., 2002.

[4] The Boeing Company. "787 Airplane Characteristics for Airport Planning", Retrieved April 22, 2008 from http://www.boeing.com/commercial/airports/acaps/787sec9.pdf, 2007.

[5] Y. Yorozu, M. Hirano, K. Oka, and Y. Tagawa, "Electron spectroscopy studies on magneto-optical media and plastic substrate interface," IEEE Transl. J. Magn. Japan, vol. 2, pp. 740-741, August 1987 [Digests 9th Annual Conf. Magnetics Japan, p. 301, 1982].

[6] M. Young, The Technical Writer's Handbook. Mill Valley, CA: University Science, 1989.